



Cite this: *Chem. Sci.*, 2023, **14**, 12645

All publication charges for this article have been paid for by the Royal Society of Chemistry

Reversible Cl/Cl^- redox in a spinel Mn_3O_4 electrode[†]

Sean K. Sandstrom,^{‡,a} Qiuyao Li,^{‡,b} Yiming Sui,^{‡,a} Mason Lyons,^c Chun-Wai Chang,^c Rui Zhang,^d Heng Jiang,^a Mingliang Yu,^a David Hoang,^a William F. Stickle,^e Huolin L. Xin,^{*,d} Zhenxing Feng,^{*,d} De-en Jiang,^{*,d} and Xiulei Ji,^{*,d}

A unique prospect of using halides as charge carriers is the possibility of the halides undergoing anodic redox behaviors when serving as charge carriers for the charge-neutrality compensation of electrodes. However, the anodic conversion of halides to neutral halogen species has often been irreversible at room temperature due to the emergence of diatomic halogen gaseous products. Here, we report that chloride ions can be reversibly converted to near-neutral atomic chlorine species in the Mn_3O_4 electrode at room temperature in a highly concentrated chloride-based aqueous electrolyte. Notably, the Zn^{2+} cations inserted in the first discharge and trapped in the Mn_3O_4 structure create an environment to stabilize the converted chlorine atoms within the structure. Characterization results suggest that the Cl/Cl^- redox is responsible for the observed large capacity, as the oxidation state of Mn barely changes upon charging. Computation results corroborate that the converted chlorine species exist as polychloride monoanions, *e.g.*, $[\text{Cl}_3]^-$ and $[\text{Cl}_5]^-$, inside the Zn^{2+} -trapped Mn_3O_4 , and the presence of polychloride species is confirmed experimentally. Our results point to the halogen plating inside electrode lattices as a new charge-storage mechanism.

Received 30th August 2023
Accepted 9th October 2023

DOI: 10.1039/d3sc04545e
rsc.li/chemical-science

Introduction

As the world continues to shift away from fossil fuels toward renewable energy sources, there is an ever-growing demand for energy-storage solutions that are safe, low-cost, and use abundant and environmentally benign material resources.^{1–3} Unfortunately, the current Li-ion batteries are lacking in each of these considerations.^{4,5} Thus, immense efforts have been devoted to other more sustainable battery systems, *e.g.*, Na-ion,^{6,7} K-ion,^{8,9} and Zn-ion batteries.^{10–12} Beyond these systems that operate *via* the reversible (de)insertion of cation charge carriers in electrode hosts, more recently, systems that use anions as the ion charge carriers have begun to attract significant interest.^{13,14} These so-called anion-shuttle batteries, including dual-ion batteries¹⁵

and anion rocking-chair batteries,^{16,17} are attractive due to their potentially high energy densities and low costs, as well as resource availability.

A unique feature of using anionic charge carriers is the possibility of the anions undergoing anodic reactions to form neutral species, which can be deemed as plating of non-metals. Redox of Cl^- , for example, has been studied and utilized in batteries since the 19th century.¹⁸ However, the Cl_2/Cl^- redox process generally suffers from poor reversibility due to loss of gaseous Cl_2 .^{19–25} Recently, Dai *et al.* demonstrated $\text{Cl}_2||$ alkali metal batteries that operate *via* the reversible Cl_2/Cl^- redox at carbon-based electrodes.^{26,27} The effective trapping of Cl_2 as the charge product at the electrode hosts was deemed essential in affording the reversibility of these systems. Wang *et al.* showed high reversibility of the Cl_2/Cl^- redox couple in an aqueous NaCl electrolyte by storing the as-produced Cl_2 in nonaqueous, water-immiscible phases such as CCl_4 .²⁸ Other approaches for overcoming the loss of gaseous Cl_2 include the formation of interhalogen species with higher boiling points, *e.g.*, BrCl and ICl , or operating the electrode below the boiling point of Cl_2 liquid.^{29–33}

Another approach for avoiding the escape of gaseous Cl_2 , which has yet to be explored, would be to “plate” neutral Cl atoms inside a host material. Such a mechanism would require a host material to effectively anchor the plated Cl atoms, where the strong binding between the inserted Cl and the host inhibits the formation of the Cl–Cl diatomic bond. Our group recently

^aDepartment of Chemistry, Oregon State University, Corvallis, OR, 97331, USA. E-mail: david.ji@oregonstate.edu

^bInterdisciplinary Materials Science Program, Vanderbilt University, Nashville, TN, 37235, USA. E-mail: de-en.jiang@vanderbilt.edu

^cSchool of Chemical, Biological, and Environmental Engineering, Corvallis, OR, 97331, USA. E-mail: zhenxing.feng@oregonstate.edu

^dDepartment of Physics and Astronomy, University of California, Irvine, CA, 92697, USA. E-mail: huolin.xin@uci.edu

^eHewlett-Packard Co., Corvallis, OR, 97330, USA

[†] Electronic supplementary information (ESI) available. See DOI: <https://doi.org/10.1039/d3sc04545e>

[‡] These authors contributed equally to this work.



reported on the reversible anodic charge-storage behaviors of a spinel Mn_3O_4 electrode after trapping Zn^{2+} cations in the first discharge in a concentrated ZnCl_2 -based electrolyte.³⁴ After Zn^{2+} is trapped, the as-formed $\text{Zn}_{0.25}\text{Mn}_3\text{O}_4$ electrode exhibited a specific charge capacity of over 200 mA h g^{-1} with an average operating potential above 1.6 V vs. Zn^{2+}/Zn . Herein, we report that the large capacity observed in the charging process is not due to the oxidation of Mn-ions of Mn_3O_4 , where the oxidation state of Mn remains nearly unchanged during cycling, but from a conversion from chloride to partially charged polychloride species stored in the distorted lattice of the Mn_3O_4 cathode.

Results and discussion

Electrochemical performance of the Mn_3O_4 electrode

The electrochemical performance of the Mn_3O_4 (space group, $I4_1/\text{amd}$, PDF # 24-0734, Fig. S1†)^{34,35} electrode was first evaluated using a concentrated aqueous water-in-salt electrolyte (WiSE) of 20 M ZnCl_2 + 5 M NH_4Cl . As reported before, when cycled in a two-electrode cell with Zn metal as the counter and reference electrode, the Mn_3O_4 electrode demonstrates a relatively small first discharge capacity of 128 mA h g^{-1} at a potential of ~0.6 V (vs. Zn^{2+}/Zn and hereafter) and a current rate of 50 mA g^{-1} (Fig. 1a).³⁴ The subsequent charging process results in a substantially larger capacity of 218 mA h g^{-1} at an average potential of 1.66 V (the potential at half the capacity). This exceedingly large hysteresis in the first cycle suggests that the initial insertion of Zn^{2+} cations is largely irreversible and that the oxidative insertion of anions was deemed responsible for most of the charging capacity. The large potential hysteresis disappears after the first cycle, and the second discharge delivers a capacity of 226 mA h g^{-1} at a slightly smaller potential

than the charging process, thereby indicating the excellent reversibility of the anion-hosting reaction. A self-discharge test was performed after the first cycle to assess the stability and reversibility of the charged electrode. After idling the charged electrode for 12 hours, the electrode delivered a Coulombic efficiency of 94.3%, suggesting the good stability and reversibility of the charge products in the electrode (Fig. S2†). Note that the first charge capacity with Zn^{2+} trapped is much larger than the case when we charged the Mn_3O_4 cathode directly with a capacity of 84 mA h g^{-1} (Fig. 1b and S3†). To further evaluate the effect of the initial Zn^{2+} -trapping process, we cycled the Mn_3O_4 electrode against an activated carbon counter electrode with another high-concentration chloride-based aqueous electrolyte of 15 M tetraethylammonium chloride (TEACl) (Fig. S4†). The initial discharge capacity was only ~13 mA h g^{-1} , indicating that the bulky tetraethylammonium cation was not inserted into Mn_3O_4 to any meaningful extent. The subsequent charge capacity was ~64 mA h g^{-1} , which is closer to when we charged the pristine Mn_3O_4 electrode first in the 20 M ZnCl_2 + 5 M NH_4Cl WiSE. This significant capacity difference suggests that the initial trapping of Zn^{2+} cations transforms the Mn_3O_4 structure in such a way that it facilitates the anodic process of anion storage. The question is: Can the trapped Zn^{2+} ions promote the storage of other anions?

We also investigated the redox behaviors of the Mn_3O_4 electrode in common aqueous Zn-ion electrolytes of 2 M ZnSO_4 and 2 M $\text{Zn}(\text{ClO}_4)_2$. In both electrolytes, the Mn_3O_4 electrode also exhibits a low-potential plateau around 0.4 V in the first discharge. However, the Mn_3O_4 electrode showed two apparent charge plateaus in these electrolytes, with the first plateau at potentials well below 1.66 V, the potential in the chloride-based WiSE (Fig. 1c and d). This two-plateau behavior is commonly observed for manganese oxide cathodes in mildly acidic aqueous electrolytes and is often attributed to H^+ and Zn^{2+} coininsertion^{36,37} or a combination of Zn^{2+} (de)insertion and $\text{MnO}_x/\text{Mn}^{2+}$ dissolution/deposition reactions.³⁸ The distinctly different redox behaviors of the Mn_3O_4 electrode in the chloride-based electrolyte and the non-chloride electrolytes are also displayed in the cyclic voltammetry (CV) curves, where Mn_3O_4 exhibits two distinct pairs of redox peaks in the 2 M ZnSO_4 in contrast to one pair in the chloride WiSE (Fig. S5†). We conducted inductively coupled plasma optical emission spectroscopy (ICP-OES) after the second discharge, where the dissolved concentration of Mn in the ZnSO_4 electrolyte corresponds to 3.6 times the observed discharge capacity. However, in the ZnCl_2 WiSE electrolyte, the dissolution of Mn could only account for 4.3% of the observed discharge capacity. The results suggest that the operation of Mn_3O_4 in dilute electrolytes such as 2 M ZnSO_4 occurs by the dissolution of Mn-ions and deposition of manganese oxides, where the Zn-trapping and the associated promoted anion storage are irrelevant.

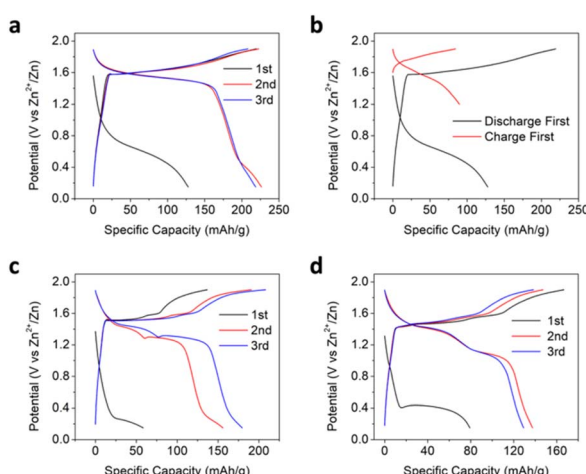


Fig. 1 (a) Galvanostatic charge–discharge (GCD) potential profiles of the Mn_3O_4 electrode in the 20 M ZnCl_2 + 5 M NH_4Cl WiSE. (b) Comparison of the first cycle GCD profiles of the Mn_3O_4 electrode in the WiSE when it is discharged first to a lower cutoff potential of 0.2 V and when it is charged first with the lower cutoff potential raised to 1.2 V to eliminate Zn^{2+} insertion. GCD profiles of the Mn_3O_4 electrode in common aqueous Zn-ion electrolytes of (c), 2 M ZnSO_4 and (d), 2 M $\text{Zn}(\text{ClO}_4)_2$.

Characterization of the operation of the Mn_3O_4 electrode in the ZnCl_2 -based WiSE electrode

Ex situ X-ray diffraction (XRD) results indicate significant amorphization of the Mn_3O_4 structure after the initial Zn^{2+}



insertion (Fig. S6†). This loss in the long-range order could explain how the relatively large Cl^-/Cl anions/atoms are able to be lodged within the compact structure after the following charge. The energy dispersive X-ray spectroscopy (EDS) elemental mapping associated with TEM confirms the Zn^{2+} insertion inside the structure of Mn_3O_4 after the initial discharge (Fig. 2a). Interestingly, the Zn content appears to be particularly enriched towards the surface of the Mn_3O_4 particles. Indeed, the high-angle annular dark field scanning transmission electron microscopy (HAADF-STEM) images indicate that the surface of the Mn_3O_4 particle is furnished with Zn^{2+} cations rather than O^{2-} anions after discharging (Fig. 2b). Elemental mapping obtained after the subsequent charging process shows a uniform increase in Cl content, thereby indicating the insertion of Cl^-/Cl anions/atoms (Fig. 2c). Of note, the Zn content is significantly more concentrated at the Mn_3O_4 surface after the charging process, as shown by the EDS mapping and the associated line scanning profile, which indicates that the inserted Zn^{2+} cations become trapped towards the surface of the particle (Fig. 2c and S7†) and the trapped Zn^{2+} cations are not static during cycling.

To reveal the charge storage mechanism of the Mn_3O_4 electrode in the chloride-based WiSE, we examined the Mn oxidation state at different state of charge (SoC) using *ex situ* synchrotron-based X-ray absorption spectroscopy (XAS).^{39–41} The Mn K-edge X-ray absorption near-edge structure (XANES) studies showed slight changes in the edge positions from the pristine, to the discharged, and charged samples (Fig. 3a and S8†). From fully discharged to fully charged in the first cycle, the valence state of Mn was calculated to increase by +0.09 (from $\text{Mn}^{2.83+}$ to $\text{Mn}^{2.92+}$). In theory, such an oxidation state change would result in a small specific capacity of only 31.6 mA h g^{-1} . However, we obtained a much larger specific capacity of 218 mA h g^{-1} for the first charge of the Mn_3O_4 electrode (Fig. 1a). These very subtle changes in the oxidation state of Mn were corroborated by X-ray photoelectron spectroscopy (XPS), where the calculated oxidation states of Mn in the spectra of the pristine and charged electrodes were +2.63 and +2.75, respectively (Fig. 3b). Moreover, there were no obvious differences in the soft XAS (sXAS) spectra of Mn between the pristine, discharged, and charged samples (Fig. 3c), further indicating the

lack of significant Mn redox involved in the charge storage mechanism of the Mn_3O_4 electrode in the chloride WiSE. This absence of the Mn redox in the (dis)charge processes of the Mn_3O_4 electrode supports the possibility of Cl/Cl^- redox as being the major contributor to the observed capacity because only Cl^- and water can be oxidized in the charging process other than Mn, where Cl^- should be oxidized before water due to its lower redox potential at such a high concentration.

Effect of Zn^{2+} -trapping on Cl/Cl^- plating/stripping and the generation of polychloride anions

To gain a theoretical understanding of how the initial Zn^{2+} -trapping process facilitates the subsequent Cl^-/Cl hosting and redox reaction, we conducted density functional theory (DFT) calculations to investigate the behavior of Cl insertion in Mn_3O_4 before and after Zn trapping. Fig. 4a and b exhibit the configurations with Zn inserted into the octahedral (Oh) site (denoted as ZnOh) and the tetrahedral (Td) site (denoted as ZnTd) of Mn_3O_4 , respectively. We found that the Td site is slightly more energetically favorable by 0.12 eV than the Oh site for Zn. During geometry optimization, the Mn atoms adjacent to Zn spontaneously move from the Td sites to Oh sites, leading to the formation of a layer of Td-site vacancies, resulting in a characteristic of spinel-to-layered structure transformation. This structural transformation results in a deformation of the crystal structure, accompanied by a volume expansion of approximately 4%. The calculated insertion energy of Zn into Mn_3O_4 is –1.0 eV (Table S1†), suggesting the stability of the structure after the initial Zn-trapping process.

Subsequently, we studied the behavior of Cl insertion in Mn_3O_4 following the initial Zn-trapping process. Interestingly, upon comparing the energetics of various potential Cl intercalation sites, the computation results suggest the formation of polychloride monoanions within the structures. Specifically, within the ZnOh model, the inserted Cl atoms form trichloride $[\text{Cl}_3]^-$ anions, while within the ZnTd model, they formed T-shaped pentachloride $[\text{Cl}_5]^-$ anions (Fig. 4d, e, and S9†).^{42–47} This unique finding sheds light on a new mechanism of Cl storage. The presence of these polychloride species helps explain the stability of “plated” chlorine species within the

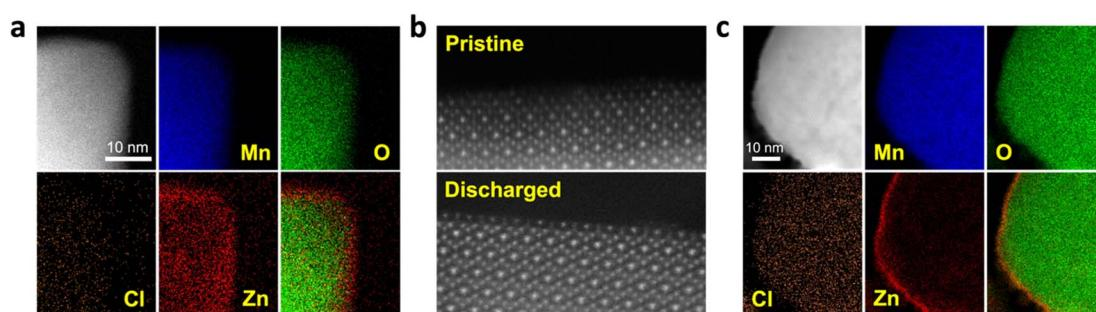


Fig. 2 (a) An HAADF-STEM image of the Mn_3O_4 electrode and associated EDS elemental mappings of the Mn, O, Cl, and Zn contents after the first discharge. (b) HAADF-STEM images of the near-surface region of the Mn_3O_4 before and after the first discharge, where the surface of the Mn_3O_4 is furnished with Zn-ions after the first discharge. (c) HAADF-STEM image of the Mn_3O_4 electrode and associated elemental mappings of the Mn, O, Cl, and Zn contents after the first charge.



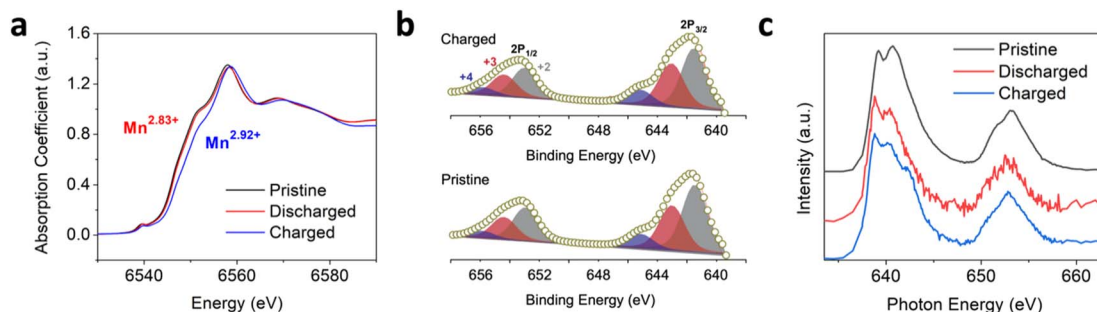


Fig. 3 (a) Normalized XANES of the Mn K-edge spectra of the pristine Mn_3O_4 electrode and the Mn_3O_4 electrode after the initial discharge and charge. The calculated oxidation state changes from +2.83 to +2.92 from the fully discharged to the fully charged state of the Mn_3O_4 electrode in the first cycle. (b) XPS spectra of the charged (upper) and pristine (lower) Mn_3O_4 electrode with Mn 2p_{3/2} and Mn 2p_{1/2} profiles. (c) Mn L-edge sXAS spectra of the pristine, discharged, and charged Mn_3O_4 electrodes.

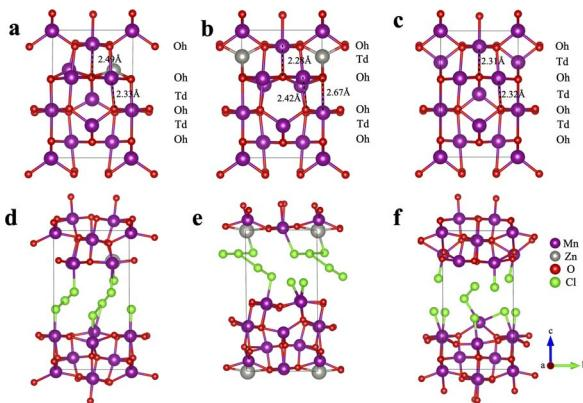


Fig. 4 (a) The optimized structure of Zn trapped in the octahedral site in Mn_3O_4 (denoted as ZnOh). (b) The optimized structure of Zn trapped in the tetrahedral site in Mn_3O_4 (denoted as ZnTd). (c) The structure of pristine Mn_3O_4 . (d–f) Optimized structures upon Cl insertion into ZnOh, ZnTd, and pristine Mn_3O_4 , respectively. The stoichiometry is $\text{Zn}_{0.25}\text{Mn}_3\text{O}_4\text{Cl}_{1.75}$ for the Zn-trapped models and $\text{Mn}_3\text{O}_4\text{Cl}_{1.75}$ for the pristine Mn_3O_4 model.

crystal structure at room temperature. Notably, the oxidation of chloride into polychlorides has been demonstrated to be thermodynamically favorable in highly concentrated acidic chloride.⁴⁷ In our work, the WiSE electrolyte used is both highly acidic and features a high chloride concentration, making the oxidation of chloride into polychloride anions feasible. In contrast, for the pristine Mn_3O_4 structure without Zn-trapping, only a small amount of dichlorides (Cl_2) was formed after the insertion of Cl atoms (Fig. S9†). This finding provides an explanation for the considerably lower capacity observed in the pristine Mn_3O_4 electrode (Fig. 1b) in comparison to the Zn-trapped electrode. Furthermore, all three crystal structures experience significant volume expansion exceeding 40% upon Cl insertion. This substantial volume expansion may contribute to the observed amorphization suggested by the *ex situ* XRD patterns after cycling the electrode (Fig. S6†).

In order to assess the impact of the initial Zn-trapping on the Cl insertion process, we calculated the Cl insertion energy. Remarkably, the Cl insertion energies for the Zn-trapped

models were found to be much lower compared to the pristine Mn_3O_4 model (1.9, 2.0, and 4.0 eV for the ZnOh, ZnTd, and Mn_3O_4 models, respectively). This observation indicates that the initial Zn-trapping process plays a crucial role in facilitating the oxidation of Cl^- ions and the formation/insertion of polychloride ions, thus resulting in an enhancement in Cl storage capacity.

In addition, the hosting of these polychloride anions may explain the slight oxidation of Mn observed in the XAS and XPS spectra of the charged electrode. While the majority of the observed capacity can be attributed to the redox of the inserted Cl^- species, a slight oxidation of Mn occurs to accommodate the negatively charged polychloride monoanions (Fig. 3a–c). This observation of slight oxidation in Mn aligns with the findings from the Bader charge analysis,⁴⁸ where a slight increase in the Bader charge of Mn is observed after Cl insertion (Table S2†). Moreover, the COHP (crystal orbital Hamilton population) analysis⁴⁹ reveals the contribution of antibonding states near the Fermi level to the Mn–Cl bonds in the ZnOh and ZnTd models in contrast to the pristine Mn_3O_4 model. This demonstrates that the chemical bonding between Mn and Cl is weaker in the Zn-trapped models, suggesting a facile extraction of Cl^- species after Zn^{2+} -trapping (Fig. S11†).

To confirm the formation and hosting of the polychloride monoanions predicted by the calculations, we conducted ultraviolet-visible (UV-vis) spectroscopy on the electrolyte after the charging process. Surprisingly, there was no noticeable difference between the spectra of the 20 M ZnCl_2 + 5 M NH_4Cl WiSE before and after charging the Mn_3O_4 electrode. This may be due to the strong binding between the polychloride monoanions and the host structure, considering the excellent self-discharge performance. Another explanation is that any diffused-out polychloride would have reacted with the Zn metal counter electrode before being detected by the UV-vis measurement of the electrolyte.⁵⁰ To address the issue, we conducted the UV-vis on another highly concentrated chloride-based aqueous electrolyte of 15 M TEACl before and after charging the Mn_3O_4 electrode with an activated carbon free-standing film as the counter electrode (Fig. 5a). After charging, a broad peak appeared at ~ 270 nm by the electrolyte, which is very likely indicative of the $[\text{Cl}_3]^-$ anion.^{51,52} To further

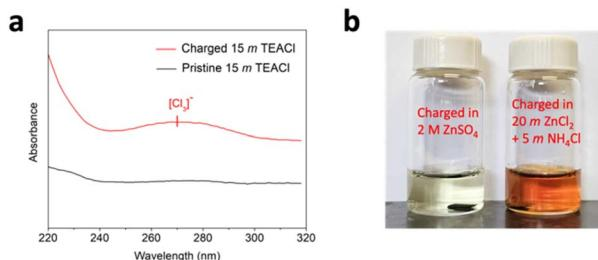


Fig. 5 (a) UV-vis spectra of the pristine 15 M TEACl electrolyte and the 15 M TEACl electrolyte after the Mn_3O_4 electrode was charged in this electrolyte. (b) The 0.5 M KI solutions after immersing the Zn^{2+} -trapped Mn_3O_4 electrode after charging in the 2 M $ZnSO_4$ electrolyte (left) and after charging in the 20 M $ZnCl_2$ + 5 M NH_4Cl WiSE (right).

confirm the existence of the polychloride monoanions formed with the Mn_3O_4 structure after charging in the 20 M $ZnCl_2$ + 5 M NH_4Cl WiSE, we immersed the fully charged Mn_3O_4 electrode in an aqueous solution of 0.5 M KI. It was observed that the color of the KI solution quickly turned brownish, thereby indicating the presence of the polychloride monoanions as the charge products with the Mn_3O_4 host (Fig. 5b). In stark contrast, when the Mn_3O_4 electrode charged in the 2 M $ZnSO_4$ electrolyte was immersed in the KI solution, the color of the solution did not change.

Conclusions

In summary, we have demonstrated and characterized a new charge storage mechanism of reversible Cl/Cl^- “plating/stripping” at a spinel Mn_3O_4 electrode in a high-concentration chloride-based aqueous electrolyte. The initial irreversible insertion of Zn^{2+} cations transforms the Mn_3O_4 structure in such a way that it helps facilitate the subsequent reversible Cl/Cl^- redox reactions. The Mn_3O_4 host acts as a “semi-catalyst” that allows the oxidation of Cl^- to Cl but not to Cl_2 gas. Characterization by EDS, XAS, and XPS spectroscopies confirms that Mn redox is not responsible for most of the observed capacity. Instead, computation and experimental results suggest that the oxidized Cl^- anions preferentially form polychloride monoanions when hosted within the Zn^{2+} -trapped Mn_3O_4 . Our results present a new strategy to use semi-catalysts as electrode materials that can effectively facilitate reversible Cl/Cl^- “plating/stripping” reactions at room temperature.

Experimental

Chemicals and materials

Nanoscale hausmannite Mn_3O_4 powder was synthesized by a room-temperature precipitation method.^{34,35} To begin, 1.126 g of $MnSO_4 \cdot H_2O$ (Alfa Aesar) was dissolved into 150 mL of deionized (DI) water. The aqueous $MnSO_4$ solution was then titrated with 29% NH_4OH solution *via* dropwise additions under magnetic stirring until it reached a pH of 11. Once the solution was at pH 11, it was left to react under magnetic stirring for 1 h before being stored overnight at room temperature.

The brown precipitate was then washed with DI water and centrifuged until a pH of 7 was obtained. Lastly, the precipitate was dried at 80 °C overnight to obtain the final Mn_3O_4 powder.

For the preparation of the 20 M $ZnCl_2$ + 5 M NH_4Cl WiSE, anhydrous zinc chloride (metals basis, 99.95%) was purchased from Thermo Scientific. Ammonium chloride (ACS, 99.5%) and the water (HPLC grade) were purchased from Alfa Aesar.

Electrochemical measurements

Electrochemical tests were done using Swagelok cells. The Mn_3O_4 working electrodes were composed of 70 wt% active mass, 20 wt% KetjenBlack, and 10 wt% polyvinylidene fluoride binder coated on carbon fiber paper current collectors. The typical active mass loading was ~ 2 mg cm^{-2} . The Mn_3O_4 free-standing film electrodes used for obtaining the *ex situ* XRD patterns, self-discharge experiments, and the KI solution immersion tests were composed of 70 wt% active mass, 20 wt% KetjenBlack, and 10 wt% polytetrafluoroethylene (PTFE) binder. GCD measurements were obtained using a LANDT Battery Test System CT3002A, and CV tests were conducted with a VMP-3 multi-channel workstation.

Materials characterization

XRD patterns were obtained using a Rigaku Ultima IV diffractometer with $Cu K\alpha$ radiation ($\lambda = 1.5406 \text{ \AA}$) at a scan rate of 1° per minute. TEM data were recorded on an aberration-corrected (scanning) transmission electron microscope operated at 300 keV with a cold field-emission source (JEM-ARM300F Grand ARM). The energy dispersive X-ray spectroscopic (EDS) data were taken with dual 100 mm² silicon drift detectors (SDD). Hard XAS was performed at the Advanced Photon Source 10-BM in transmission mode. XAS data was processed using Athena for pre-edge background subtraction and normalization. The Mn oxidation state was determined with XANES edge position at a normalized absorbance of 0.5 and linearly interpolated with Mn_3O_4 and Mn_2O_3 standards as +2.67 (6544.8 eV) and +3 (6548.7 eV) oxidation states, respectively. sXAS at Mn L-edge was performed using total electron yield (TEY) mode at beamline 7.3.1 of Advanced Light Source (ALS) of Lawrence Berkeley National Laboratory (LBNL).

For XPS, a Physical Electronics Quantera II Hybrid was used for the analysis. The system energy scale was calibrated to $Cu 2p_{3/2}$ at 932.6 eV and $Au 4f$ at 84.0 eV. The base pressure of the system was 3×10^{-7} Pa. The XPS experiments were measured on as-loaded samples at room temperature. XPS was performed using monochromatized $Al K\alpha$ radiation ($h\nu = 1486.6$ eV, at 50 watts and 100 μm beam diameter). The electron analyzer pass energy was set to 69 eV, with an emission angle of 45°. The specimens were neutralized using a combination of an electron flood gun set to 0.6 eV at 20 μA and an ion flood gun set to 0.1 kV. The XPS data were charge corrected to the C 1s aliphatic carbon binding energy at 284.8 eV. The XPS spectra were analyzed by fitting using CasaXPS software.

UV-vis spectroscopy analyses of the electrolytes were performed using a UV-vis-NIR spectrophotometer (PerkinElmer Lambda 750).

Theoretical calculations

DFT calculations were performed *via* the Vienna *ab initio* simulation package (VASP).⁵³ The ion–electron interaction was depicted with the projector augmented wave (PAW) method. The electron exchange correlation was described by the Perdew, Burke, and Ernzerhof (PBE) functional with generalized gradient approximation (GGA).⁵⁴ The cutoff energy of the plane-wave basis set was set to 450 eV. The Brillouin zone was sampled by $(3 \times 3 \times 2)$ Γ -centered k -point mesh. The valence electrons of Mn, Zn, O, and Cl are $3d^54s^2$, $3d^{10}4s^2$, $2s^2sp^4$, and $3s^23p^5$, respectively. The convergence threshold for structural optimization and electronic energy was set to be 0.01 eV \AA^{-1} in force and 1×10^{-5} eV, respectively. The unit cell and atomic position were allowed to relax along with structure optimization. Spin polarization was considered in all computations. The DFT + U method was employed as the correction to simulate the strongly correlated materials, including transition metals.⁵⁵ The values of U and J for Mn were set to be 4.5 and 0.5 eV, respectively.^{56,57}

In this work, the crystal structures were visualized using VESTA.⁵⁸ The atomic net charge was generated with code developed by Henkelman's group *via* the Bader charge analysis.⁴⁸ The crystal orbital Hamilton population (COHP) analysis was obtained using LOBSTER to analyze the chemical bond.⁴⁹

The insertion energy of Zn (ΔE_{Zn}) and the insertion energy of Cl (ΔE_{Cl}) were calculated by the following equations:

$$\Delta E_{\text{Zn}} = E(\text{Bulk} + \text{Zn}) - E(\text{Bulk}) - E(\text{Zn}) \quad (1)$$

$$\Delta E_{\text{Cl}} = E(\text{Bulk} + n \times \text{Cl}) - E(\text{Bulk}) - n \times 0.5E(\text{Cl}_2) \quad (2)$$

where $E(\text{Bulk} + \text{Zn})$ is the total energy of the Mn_3O_4 unit cell with interstitial Zn atom and $E(\text{Bulk})$ and $E(\text{Bulk} + n \times \text{Cl})$ represent the total energy of a Mn_3O_4 unit cell with or without interstitial Zn atom and that contain n interstitial Cl atoms, respectively. $E(\text{Zn})$ and $E(\text{H}_2)$ represent the energy of a Zn atom and one H_2 molecule in a vacuum, respectively.

According to previous studies, the magnetic ordering of the Mn_3O_4 unit cell was set to be $(\uparrow\uparrow\downarrow\downarrow\uparrow\uparrow)$.⁵⁹

Data availability

Additional characterization and computation results are provided in the ESI.†

Author contributions

S. K. Sandstrom: investigation, formal analysis, visualization, data curation, writing – original draft. Q. Li: investigation, formal analysis, visualization, data curation. M. Lyons: investigation, formal analysis, data curation. C.-W. Chang: investigation, formal analysis, data curation. R. Zhang: investigation, formal analysis, data curation. Y. Sui: investigation, formal analysis, data curation. H. Jiang: investigation. M. Yu: investigation. D. Hoang: investigation. W. F. Stickle: investigation, formal analysis, data curation. H. L. Xin: funding acquisition, writing – review and editing, supervision. Z. Feng: funding acquisition, writing – review and editing, supervision. D. Jiang:

funding acquisition, writing – review and editing, supervision. X. Ji: conceptualization, funding acquisition, writing – review and editing, supervision.

Conflicts of interest

There are no conflicts to declare.

Acknowledgements

X. J. and D. J. thank the U.S. National Science Foundation (NSF) for the financial support with the Awards DMR 2221645 and DMR 2221646. M. L., C.-W. C. and Z. F. thank the U.S. NSF for financial support from CBET 2016192 and CBET 1949870. The hard XAS measurements were done at beamline 10-BM of The Materials Research Collaborative Access Team (MRCAT) at the Advanced Photon Source. MRCAT operations are supported by the Department of Energy (DOE) and the MRCAT member institutions. This research used resources of the Advanced Photon Source; a U.S. DOE Office of Science User Facility operated for the DOE Office of Science by Argonne National Laboratory under Contract No. DE-AC02-06CH11357. The soft X-ray absorption spectroscopy measurements were performed at beamline 6.3.1 of Advanced Light Source, which is an Office of Science User Facility operated for the U.S. DOE Office of Science by Lawrence Berkeley National Laboratory and supported by the DOE under Contract No. DEAC02-05CH11231. The UCI experiments were supported by the Office of Basic Energy Sciences of the U.S. Department of Energy, under award no. DE-SC0021204. R. Z.'s effort on this project was supported by HLX's startup funding. The authors thank Jesse M. Muratli and the Keck Collaboratory for Plasma Spectrometry at Oregon State University for ICP-OES measurements.

Notes and references

- 1 J. Song, K. Xu, N. Liu, D. Reed and X. Li, *Mater. Today*, 2021, **45**, 191–212.
- 2 C. Bauer, S. Burkhardt, N. P. Dasgupta, L. A.-W. Ellingsen, L. L. Gaines, H. Hao, R. Hischier, L. Hu, Y. Huang, J. Janek, C. Liang, H. Li, J. Li, Y. Li, Y.-C. Lu, W. Luo, L. F. Nazar, E. A. Olivetti, J. F. Peters, J. L. M. Rupp, M. Weil, J. F. Whitacre and S. Xu, *Nat. Sustain.*, 2022, **5**(3), 176–178.
- 3 J. B. Goodenough and Y. Kim, *Chem. Mater.*, 2010, **22**, 587–603.
- 4 K. Turcheniuk, D. Bondarev, V. Singhal and G. Yushin, *Nature*, 2018, 467–470.
- 5 W. Tahil, *Implications of Future PHEV Production for Lithium Demand*, Martainville: Meridian International Research, 2007.
- 6 S. Y. Hong, Y. Kim, Y. Park, A. Choi, N.-S. Choi and K. T. Lee, *Energy Environ. Sci.*, 2013, **6**(7), 2067–2081.
- 7 Q. Li, Q. Wei, W. Zuo, L. Huang, W. Luo, Q. An, V. O. Pelenovich, L. Ma and Q. Zhang, *Chem. Sci.*, 2017, **8**(1), 160–164.
- 8 W. Zhang, Y. Liu and Z. Guo, *Sci. Adv.*, 2019, **5**(5), eaav7412.



9 J. Mao, C. Wang, Y. Lyu, R. Zhang, Y. Wang, S. Liu, Z. Wang, S. Zhang and Z. Guo, *J. Mater. Chem. A*, 2022, **10**(37), 19090–19106.

10 L. Cao, D. Li, T. Pollard, T. Deng, B. Zhang, C. Yang, L. Chen, J. Vatamanu, E. Hu, M. J. Hourwitz, L. Ma, M. Ding, Q. Li, S. Hou, K. Gaskell, J. T. Fourkas, X.-Q. Yang, K. Xu, O. Borodin and C. Wang, *Nat. Nanotechnol.*, 2021, **16**(8), 902–910.

11 D. Dong, T. Wang, Y. Sun, J. Fan and Y.-C. Lu, *Nat. Sustainability*, 2023, 1–11.

12 D. Zhao, X. Pu, S. Tang, M. Ding, Y. Zeng, Y. Cao and Z. Cheng, *Chem. Sci.*, 2023, **14**(30), 8206–8213.

13 S. K. Sandstrom, X. Chen and X. Ji, *Carbon Energy*, 2021, **3**(4), 627–653.

14 Q. Liu, Y. Wang, X. Yang, D. Zhou, X. Wang, P. Jaumaux, F. Kang, B. Li, X. Ji and G. Wang, *Chem.*, 2021, **7**(8), 1993–2021.

15 F. P. McCullough, C. A. Levine and R. V. Snelgrove, *US Pat.*, 4830938, 1989.

16 M. A. Reddy and M. Fichtner, *J. Mater. Chem.*, 2011, **21**(43), 17059–17062.

17 X. Zhao, S. Ren, M. Bruns and M. Fichtner, *J. Power Sources*, 2014, **245**, 706–711.

18 L. Winter and G. Degner, *Minute Epics of Flight*, 1933.

19 J. Jorné, J. T. Kim and D. Kralik, *J. Appl. Electrochem.*, 1979, **9**, 573–579.

20 D. L. Thomas and D. N. Bennion, *J. Electrochem. Soc.*, 1989, **136**(12), 3553.

21 C. F. Holmes, *Batteries for Implantable Biomedical Devices*, 1986, pp. 133–180.

22 J. T. Kim and J. Jorné, *J. Electrochem. Soc.*, 1977, **124**(10), 1473.

23 J. T. Kim and J. Jorné, *J. Electrochem. Soc.*, 1980, **127**(1), 8.

24 K. A. Klinedinst and M. J. Domeniconi, *J. Electrochem. Soc.*, 1980, **127**(3), 539.

25 P. R. Gifford and J. B. Palmisano, *J. Electrochem. Soc.*, 1988, **135**(3), 650.

26 G. Zhu, X. Tian, H.-C. Tai, Y.-Y. Li, J. Li, H. Sun, P. Liang, M. Angell, C.-L. Huang, C.-S. Ku, W.-H. Hung, S.-K. Jiang, Y. Meng, H. Chen, M.-C. Lin, B.-J. Hwang and H. Dai, *Nature*, 2021, **596**(7873), 525–530.

27 G. Zhu, P. Liang, C.-L. Huang, C.-C. Huang, Y.-Y. Li, S.-C. Wu, J. Li, F. Wang, X. Tian, W.-H. Huang, S.-K. Jiang, W.-H. Hung, H. Chen, M.-C. Lin, B.-J. Hwang and H. Dai, *J. Am. Chem. Soc.*, 2022, **144**(49), 22505–22513.

28 S. Hou, L. Chen, X. Fan, X. Fan, X. Ji, B. Wang, C. Cui, J. Chen, C. Yang, W. Wang, C. Li and C. Wang, *Nat. Commun.*, 2022, **13**(1), 1281.

29 J. Xu, T. P. Pollard, C. Yang, N. K. Dandu, S. Tan, J. Zhou, J. Wang, X. He, X. Zhang, A.-M. Li, E. Hu, X.-Q. Yang, A. Ngo, O. Borodin and C. Wang, *Joule*, 2023, **7**(1), 83–94.

30 Q. Guo, K.-I. Kim, S. Li, A. M. Scida, P. Yu, S. K. Sandstrom, L. Zhang, S. Sun, H. Jiang, Q. Ni, D. Yu, M. M. Lerner, H. Xia and X. Ji, *ACS Energy Lett.*, 2021, **6**(2), 459–467.

31 Y. Sui, M. Lei, M. Yu, A. Scida, S. K. Sandstrom, W. Stickle, T. D. O'Larey, D.-e. Jiang and X. Ji, *ACS Energy Lett.*, 2023, **8**(2), 988–994.

32 C. Yang, J. Chen, X. Ji, T. P. Pollard, X. Lü, C.-J. Sun, S. Hou, Q. Liu, C. Liu, T. Qing, Y. Wang, O. Borodin, Y. Ren, K. Xu and C. Wang, *Nature*, 2019, **569**(7755), 245–250.

33 G. Liang, B. Liang, A. Chen, J. Zhu, Q. Li, Z. Huang, X. Li, Y. Wang, X. Wang, B. Xiong, X. Jin, S. Bai, J. Fan and C. Zhi, *Nat. Commun.*, 2023, **14**(1), 1856.

34 H. Jiang and X. Ji, *Carbon Energy*, 2020, **2**(3), 437–442.

35 H. Jiang, Z. Wei, L. Ma, Y. Yuan, J. J. Hong, X. Wu, D. P. Leonard, J. Holoubek, J. J. Razink, W. F. Stickle, F. Du, T. Wu, J. Lu and X. Ji, *Angew. Chem.*, 2019, **131**(16), 5340–5345.

36 W. Sun, F. Wang, S. Hou, C. Yang, X. Fan, Z. Ma, T. Gao, F. Han, R. Hu, M. Zhu and C. Wang, *J. Am. Chem. Soc.*, 2017, **139**(29), 9775–9778.

37 Y. Jin, L. Zou, L. Liu, M. H. Engelhard, R. L. Patel, Z. Nie, K. S. Han, Y. Shao, C. Wang, J. Zhu, H. Pan and J. Liu, *Adv. Mater.*, 2019, **31**(29), 1900567.

38 X. Guo, J. Zhou, C. Bai, X. Li, G. Fang and S. Liang, *Mater. Today Energy*, 2020, **16**, 100396.

39 M. Wang and Z. Feng, *Chem. Commun.*, 2021, **57**(81), 10453–10468.

40 M. Wang and Z. Feng, *Curr. Opin. Electrochem.*, 2021, **30**, 100803.

41 M. Wang, L. Árnadóttir, Z. J. Xu and Z. Feng, *Nano-Micro Lett.*, 2019, **11**, 1–18.

42 H. Keil, K. Sonnenberg, C. Müller, R. Herbst-Irmer, H. Beckers, S. Riedel and D. Stalke, *Angew. Chem., Int. Ed.*, 2021, **60**(5), 2569–2573.

43 F. A. Redeker, H. Beckers and S. Riedel, *Chem. Commun.*, 2017, **53**(96), 12958–12961.

44 M. P. Bogaard, J. Peterson and A. D. Rae, *Acta Crystallogr., Sect. B: Struct. Crystallogr. Cryst. Chem.*, 1981, **37**(7), 1357–1359.

45 R. Brückner, H. Haller, M. Ellwanger and S. Riedel, *Chem.-Eur. J.*, 2012, **18**(18), 5741–5747.

46 J. Taraba and Z. Zak, *Inorg. Chem.*, 2003, **42**(11), 3591–3594.

47 D. Degoulange, G. Rousse and A. Grimaud, *ACS Energy Lett.*, 2023, **8**, 4397–4405.

48 W. Tang, E. Sanville and G. Henkelman, *J. Phys.: Condens. Matter*, 2009, **21**(8), 084204.

49 V. L. Deringer, A. L. Tchougréeff and R. Dronskowski, *J. Phys. Chem. A*, 2011, **115**(21), 5461–5466.

50 A. Van den Bossche, E. De Witte, W. Dehaen and K. Binnemans, *Green Chem.*, 2018, **20**(14), 3327–3338.

51 H. Sun, L. Yu, X. Jin, X. Hu, D. Wang and G. Z. Chen, *Electrochem. Commun.*, 2005, **7**(7), 685–691.

52 B. Wen, C. Yang, J. Wu, J. Liu, B. Li, J. Yang and Y. Liu, *ACS Energy Lett.*, 2023, **8**, 4204–4209.

53 G. Kresse and J. Furthmüller, *Phys. Rev. B: Condens. Matter Phys.*, 1996, **54**(16), 11169.

54 J. P. Perdew, K. Burke and M. Ernzerhof, *Phys. Rev. Lett.*, 1996, **77**(18), 3865.

55 V. I. Anisimov, J. Zaanen and O. K. Andersen, *Phys. Rev. B: Condens. Matter Mater. Phys.*, 1991, **44**(3), 943.

56 Y.-F. Li, S.-C. Zhu and Z.-P. Liu, *J. Am. Chem. Soc.*, 2016, **138**(16), 5371–5379.



57 Y.-F. Li and Z.-P. Liu, *J. Am. Chem. Soc.*, 2018, **140**(5), 1783–1792.

58 K. Momma and F. Izumi, *J. Appl. Crystallogr.*, 2011, **44**(6), 1272–1276.

59 C. Franchini, R. Podloucky, J. Paier, M. Marsman and G. Kresse, *Phys. Rev. B: Condens. Matter Mater. Phys.*, 2007, **75**(19), 195128.

